Tellus (2008), 60A, 141–153
Printed in Singapore. All rights reserved

TELLUS

Can polar lows lead to a warming of the ocean surface?

By O. SAETRA*, T. LINDERS and J.B. DEBERNARD, *The Norwegian Meteorological Institute, PO Box 43 blindern, 0313 Oslo, Norway*

(Manuscript received 2 April 2007; in final form 23 August 2007)

ABSTRACT

Possible surface warming by strong wind-forcing from polar lows in the North-Atlantic has been investigated using a numerical model for vertical entrainment of waters from a subsurface warm core, and microwave satellite images of sea-surface temperature during polar low events. The hypothesis is based on the frequently observed subsurface warm core in oceans influenced by the North-Atlantic current (NAC) or by outflowing surface water from the Arctic Ocean. CTD-soundings from the Nordic Seas reveal that the waters from the NAC are located under colder and less saline surface waters in winter. For sufficiently strong wind events, turbulent entrainment of this subsurface warm core may lead to a rapid surface warming. Our main findings is that the surface warming of more than 1 °C may take place within a few hours. The result is based on model runs with initial temperature and salinity profiles from CTD-observations. Observational evidence of surface temperatures that support the hypothesis are found in microwave satellite observations from a polar low event. In the case presented here, increased sea-surface temperatures between 1 and 2 °C were observed. We believe that rapid surface warming of this magnitude may be a potential positive feedback mechanism for the cyclone intensity.

1. Introduction

The main objectives of this paper is to investigate the effect of intense polar lows on the upper ocean. Our hypothesis is that vertical mixing induced by surface stresses may lead to entrainment of waters from a warm and saline core beneath the sea surface. As will be demonstrated, in the seas where polar lows are often developed, the North-Atlantic Current (NAC) subducts under colder and less saline waters and Arctic water flows on top of warmer and more saline waters. The result of this is the frequent presence of a temperature inversion in wintertime hydrographic sections in areas influenced by the NAC. By temperature inversion, we will here refer to temperatures increasing with depth in the upper ocean. If the timescale of the entrainment and subsequent surface warming is sufficiently short, a positive feedback on the cyclone intensity is possible.

Intense mesoscale cyclones known as polar lows are frequently observed over the ocean in the Atlantic sector of the Arctic. During winter, cold and extremely stable air is formed over the ice-covered areas of the Arctic. During certain synoptic-scale weather patterns cold-air outbreak may be triggered and the cold Arctic air-masses become exposed to the relatively warm ocean surface. Such conditions promote strong deep-convection and the formation of polar lows with surface winds often exceeding 30 m s^{-1}. These small violent storms have been felt by coastal communities and seafarers over the centuries and are believed to be responsible for a number of shipwrecks. Mesoscale cyclones, with horizontal length scale of less than 1000 km, are seldom possible to detect using the sparse network of synoptic observations in the Arctic. Although the phenomena has been well known among weather forecasters, the small size and relatively rapid development has until recently made them almost impossible to forecast (Rasmussen and Turner, 2003).

During the 1960s, satellite imagery revealed new insight into the life-cycle and frequency of occurrence of polar lows. It became apparent that polar lows appear in many forms from almost pure convective systems to systems that are mainly baroclinic. Satellite images of some of these mesoscale cyclones show striking similarities with tropical hurricanes, and they have been referred to by some authors as Arctic hurricanes. Nordeng and Rasmussen (1992) investigated a polar low off the coast of Finnmark in Northern-Norway where the satellite images looked remarkably similar to a tropical hurricane, with symmetric, clear spiral bands and a well-defined eye. The low was studied using conventional observations, satellite images and model simulations. They found that the low was triggered by an upper level potential vorticity anomaly in a region of strong low level baroclinicity. The low then developed into a system of deep convection with large fluxes of latent and sensible heat from the sea surface. Emanuel and Rotunno (1989) used an axisymmetric model to investigate whether Arctic hurricanes are possible over polar oceans. They also found that some polar lows show

*Corresponding author.
e-mail: oyvinds@met.no
DOI: 10.1111/j.1600-0870.2007.00279.x

similarities with tropical systems, such as large air–sea heat fluxes, deep convection and strong warming of the deep layers of the troposphere due to release of latent heat. One of the few aircraft observations ever conducted inside a polar low was reported by Shapiro et al. (1987). The NOAA P3 aircraft flew into a polar low situated in the Norwegian Sea east of Jan Mayen. Analysis showed that synoptic-scale upper-level baroclinic forcing was present in the region of the polar low spin-up. The minimum low pressure was 979 mb, and the pressure difference over 200 km was reported to be 17 mb. The observed warm core seclusion suggests that the low was in the final phase of the baroclinic evolution. Analysis also showed that the polar low had a warm inner core. Fluxes of latent and sensible heat exceeding 1000 W m^{-2} and strong upward vertical motion suggested that deep-convection and release of latent heat played an important role for energetics of the low.

The oceanic response to a moving hurricane has long been recognized (Price, 1981, 1983; Sanford et al., 1987; Brink, 1989). Entrainment of cold waters from deep layers leads to a cooling of the sea surface by a combination of extremely strong vertical mixing and large surface heat fluxes. Both model studies (Price, 1983) and observations (Sanford et al., 1987; Price et al., 1994), have revealed near-inertial oscillations in the wake of hurricanes. Zedler et al. (2002) investigated the oceans response to hurricane Felix in detail using several turbulence models for the vertical ocean mixing. The results were compared with buoy observations from the Bermuda Testbed Mooring (BTM). One of the conclusions was that the rapid surface cooling was mainly due to strong vertical mixing, and to lesser extent to the surface heat fluxes. Also Emanuel et al. (2004) used a one-dimensional model because the vertical mixing dominated the interaction.

Because of the relatively short timescale in which the surface cooling takes place, horizontal advection is of relatively minor importance. Accordingly, the cooling process could be reasonably well modelled by only taking into account the vertical mixing of momentum, heat and salt, and the surface cooling by the heat fluxes to the atmosphere.

Emanuel et al. (2004) showed that the ocean's feedback is a critical parameter limiting tropical cyclone intensity. In most hurricane models the ocean surface is still passive, not allowing for a possible feedback mechanisms due to surface cooling. Schade and Emanuel (1999) performed model experiments with an axisymmetric hurricane model a coupled to three-dimensional ocean model and demonstrated that surface cooling indeed induced a negative feedback on the tropical cyclone intensity, reducing the central pressure drop by approximately 6 hPa $^{\circ}C^{-1}$. Some recent studies focus on the possible effects of deep cores of warm waters such as the Loop Current in the Gulf of Mexico and warm-core rings (Hong et al., 2000; Shay et al., 2000). Such features act as insulation to entrainment of the cold waters under the thermocline that normally hamper further intensification of the cyclone. Strong intensification of several hurricanes have been observed as they enter the areas of the Loop current in the Gulf of Mexico. In particular Katrina, which caused large disruption to the area around New Orleans when it made landfall in August 2005, intensified into a category 5 hurricane when it entered the warm Gulf of Mexico (Kafatos et al., 2006).

The structure of this paper is as follows: In Section 2, hydrographic observations from the Nordic Seas will be investigated and the frequent presence of temperature inversions in the upper ocean during winter will be demonstrated. Section 3 gives a brief description of the one-dimensional numerical model for the vertical mixing and in Section 4 that model is validated. Section 5 presents the results of turbulent entrainment of warm waters using selected observed temperature and salinity profiles from the Nordic Seas. In Section 6, some observational evidence of rapid sea-surface warming in connection with a polar low are presented. Finally, in Section 7, a discussion of the results and some concluding remarks are given. The Appendix includes further details about the numerical model.

2. Hydrograhy of the Norwegian Sea and the Barents Sea

In the northeast Atlantic, low saline and cold Arctic water meets the high saline and warm NAC. The Arctic water enters the Nordic Seas mainly through the Fram Strait between Spitsbergen and Greenland. It flows southward, most concentrated in the western part of the region. The NAC enters the Nordic Seas mainly through the strait between Scotland and the Faraou Islands. Following the bathymetry it continues to the northeast along the edge of the Norwegian shelf. It is especially distinguishable where the slope is steep, as it is outside Lofoten, in northern Norway. Further to the north, one branch turns to the north, flowing into the Fram Strait, and one branch turns to the east deep into the Barents Sea, see Fig. 1.

The NAC current has an immense impact on the hydrography of the Arctic sector of the eastern North-Atlantic, causing ice-free conditions in large parts of the Barents Sea and the waters southwest of Spitsbergen, and leads to high sea-surface temperatures for such high latitudes in wintertime. In this area, surface temperatures around 6–7 $^{\circ}$C in January are not unusual.

The hydrography in this region is very different from the tropical oceans. Contrary to the case in low latitudes, the density differences are to a great extent caused by salinity. This opens up for the possibility of a surface layer residing on top of deeper layers of one or several degrees warmer water, without compromising stability. Especially in wintertime measurements, upper ocean temperature inversions are frequently observed in regions where the North-Atlantic Current meets polar water masses. The depth of the warm core may vary from only a few metres to 100 m or more beneath the surface.

The frequency of observed upper ocean temperature inversion during November to April is given in Fig. 1 and Tables 2–4. The statistics are based on data from HydroBase (http://www.whoi.edu/science/PO/hydrobase/). HydroBase is a

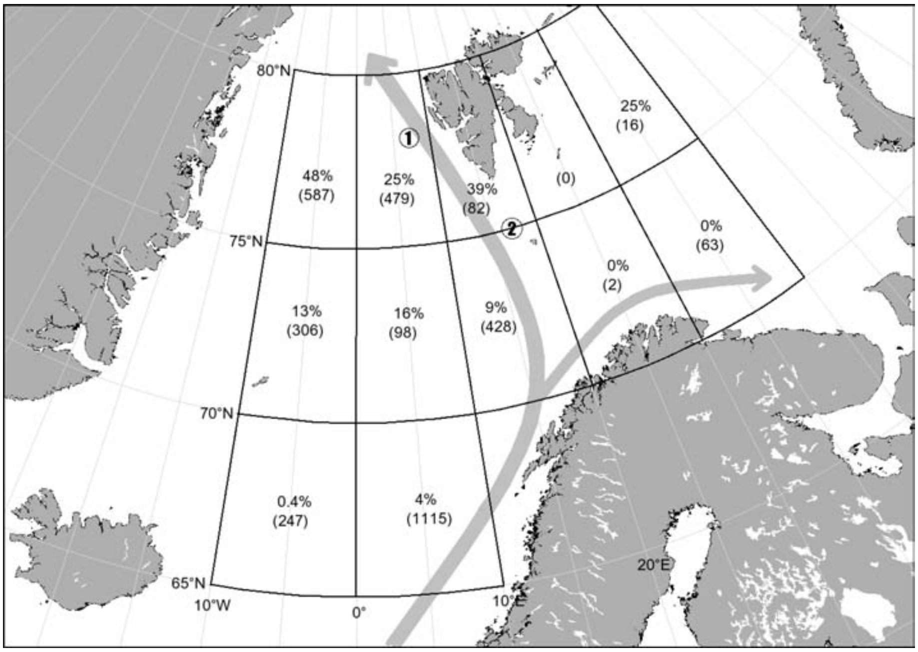

Fig. 1. The shaded arrows show schematically the path of the North Atlantic current. The percentage numbers show the frequency of observed upper ocean temperature inversion (1.0 °C down to 100 m) during November to April for respective subarea. The numbers within parenthesis show the total number of observations during November to April for respective subarea. The statistics are discussed in Section 5. Circled numbers 1 and 2 refer to stations discussed in Section 5.

Table 1. Temporal distribution of conducted measurements and frequency of observed upper ocean temperature inversion (1 °C down to 100 m). The statistics are for all the subareas depicted in Fig. 1

Month	Casts	Inversion
November	524	15%
December	106	13%
January	172	3%
February	261	9%
March	1264	17%
April	1096	22%
November–April	3423	17%

global set of raw profile data. The data are collected from several principal sources and quality controlled. The sources include World Ocean Database 2001, WOCE Hydrographic Programme, NSIDC, ICES, BarKode and various other sources. The observations used in this investigation are from the period between 1977 and 2002. Since our main interest in this investigation is the impact of strong winds from polar lows, only data for the winter months November to April have analysed here. The data distribution and statistics with all subareas included are given in Table 1.

In Fig. 1 upper ocean temperature inversion is defined as a maximum temperature in the upper 100 m of more than 1.0 °C warmer than the measurement closest to the surface, usually at 2 or 3 m depth. Statistics for 12 subareas within the region is shown. In Tables 2–4 the subareas are put into three groups depending on latitude, one group for each table. It should be noted that a majority of the measurements was done during March and April,

Table 2. Frequency of observed upper ocean temperature inversion per measuring cast from November to April. The statistics are based on measurements in the area 75°N–80°N and 10°W–40°E, see Fig. 1. Upper ocean temperature inversion is defined as an occurrence of water below the surface water and down to a specified depth, D, with a positive temperature difference to the surface water larger than a specified value, ΔT

	$D = 25$ m	$D = 50$ m	$D = 100$ m
$\Delta T = 0.5$ °C	10%	31%	47%
$\Delta T = 1.0$ °C	5%	21%	37%
$\Delta T = 1.5$ °C	2%	13%	29%
$\Delta T = 2.0$ °C	0.6%	8%	22%

Table 3. As Table 2, except the statistics are based on measurements in the area 70°N–75°N and 10°W–40°E, see Fig. 1

	$D = 25$ m	$D = 50$ m	$D = 100$ m
$\Delta T = 0.5$ °C	1%	5%	20%
$\Delta T = 1.0$ °C	0.4%	2%	11%
$\Delta T = 1.5$ °C	0.1%	0.8%	5%
$\Delta T = 2.0$ °C	0.0%	0.3%	2%

Table 4. As Table 2, except the statistics are based on measurements in the area 65°N–70°N and 10°W–10°E, see Fig. 1

	$D = 25$ m	$D = 50$ m	$D = 100$ m
$\Delta T = 0.5$ °C	2%	5%	10%
$\Delta T = 1.0$ °C	0.5%	2%	3%
$\Delta T = 1.5$ °C	0.2%	0.7%	1%
$\Delta T = 2.0$ °C	0.0%	0.4%	0.6%

and hence the statistics has a strong bias towards the conditions of these months. The great variation of measurements done in the respective subareas (numbers within parenthesis in Fig. 1) should also be noted.

Both Fig. 1 and Tables 2–4 show that upper ocean temperature inversion is a common but unevenly distributed feature in the region. A detailed analysis reveals the distinct two-component nature of the phenomenon, the two components being NAC and Arctic water. The bulk of water in the region is made up of a varying mixture of these. Inversion reflects the meeting of water with different mixtures.

The Arctic water represents the lesser volume flow into the region and it is rather quickly mixed into and diluted in the upper layers as it flows to the south. It is therefore not surprising to find the highest frequencies of inversion in the most northern subareas, where undiluted Arctic water meets bulk water with quite different properties. Arctic water is also light, which explains why inversion is more often found close to the ocean surface, see Table 2.

The NAC represents the greater volume flow into the region and its properties are closer to the properties of the bulk water of the region. Inversion resulting from the meeting of Atlantic water with bulk water are therefore less frequent and display less temperature difference (see Tables 3 and 4). Since the Atlantic water is rather heavy, the resulting inversion tends to be deeper.

Dividing the data into 2-month periods (not shown) reveals further characteristics of the influence of the Atlantic and Arctic water. However, dividing the data in this way makes some subsets of data rather small, and therefore the tendencies less significant and more disputable.

The two subareas (outlined in Fig. 1) north of 75°N and west of 10°E display a distinct dip in inversion frequency during January and February, when the outflow from the Arctic Ocean can be expected to be of lesser volume and of higher salinity. The same subareas display the highest inversion frequency during March and April, when the retracting ice cover makes the outflow from the Arctic Ocean large and of low salinity.

Studying the two subareas east of 10°E and west of 20°E reveals the influence of the North-Atlantic current. Here the pattern of temperature inversion is rather constant between November and April, actually with a tendency of more frequent inversion in January and February. This could be explained with the persistence of the North-Atlantic current, together with the generally colder bulk water during mid-winter. The subarea north of 75°N do display a rather high frequency of inversion close to the surface. But the frequency is not as high as in its two neighbouring subareas to the west, nor does this frequency display any dip in January and February or any increase in March and April.

3. Model description

For the ocean a one-dimensional model is used. Here the mean horizontal velocities, u and v, are described by the Ekman (1905) equations

$$\frac{\partial u}{\partial t} = \frac{\partial}{\partial z}\left(K_M \frac{\partial u}{\partial z}\right) + fv \tag{1}$$

and

$$\frac{\partial v}{\partial t} = \frac{\partial}{\partial z}\left(K_M \frac{\partial v}{\partial z}\right) - fu, \tag{2}$$

where t is time, K_M is the eddy viscosity and f is the Coriolis frequency, z is the vertical coordinate, with the bottom at $z = 0$ and the ocean surface at $z = H$. At the bottom there is no slip, and at the surface the boundary conditions are given by the two components of the forcing friction velocity squared, u_{*x}^2 and u_{*y}^2,

$$K_M \frac{\partial u}{\partial z} = \frac{\tau_x}{\rho}, \qquad z = H, \tag{3}$$

and

$$K_M \frac{\partial v}{\partial z} = \frac{\tau_y}{\rho}, \qquad z = H, \tag{4}$$

where τ_x and τ_y are surface stress components in x- and y-direction, respectively. Similar equations apply for the temperature, T, and the salinity, S,

$$\frac{\partial T}{\partial t} = \frac{\partial}{\partial z}\left(K_H \frac{\partial T}{\partial z}\right) + \Gamma \tag{5}$$

and

$$\frac{\partial S}{\partial t} = \frac{\partial}{\partial z}\left(K_H \frac{\partial S}{\partial z}\right), \tag{6}$$

where K_H is the eddy diffusivity and Γ is the heat from short-wave solar radiation penetrating the water column. For the temperature, the boundary condition at the surface is given by the surface heat flux, Q,

$$K_H \frac{\partial T}{\partial z} = \frac{Q}{\rho c_p}, \qquad z = H, \tag{7}$$

where ρ is the water density and c_p is the heat capacity of water. At the bottom there is no heat flux, and at both boundaries we assume no flux of salinity.

The eddy viscosity and diffusivity are calculated from the turbulent kinetic energy, k, and the turbulent mixing length, l,

$$K_M = c_\mu k^{1/2} l \qquad \text{and} \qquad K_H = c'_\mu k^{1/2} l, \tag{8}$$

where c_μ and c'_μ are stability functions, see Appendix. Following Axell and Liungman (2001), the mixing length is calculated with an algebraic expression based on the geometric length scale and the buoyancy length scale.

The equation for the turbulent kinetic energy, k, is obtained by subtracting the mean from the total kinetic energy equation, see for example Tennekes and Lumley (1972). Neglecting transport terms the k-equation reads

$$\frac{\partial k}{\partial t} = \frac{\partial}{\partial z}\left(K_M \frac{\partial k}{\partial z}\right) + P_s + P_b - \epsilon. \tag{9}$$

P_s and P_b are turbulence production from shear and from buoyancy, respectively. ϵ is the dissipation rate. The upper boundary condition is given by the injection caused by breaking waves. Following Craig and Banner (1994) this can be parametrized as

$$K_M \frac{\partial k}{\partial z} = \alpha u_*^3, \qquad z = H, \tag{10}$$

where α is a wave factor. At the bottom the logarithmic region of the law of the wall yields no flux.

The surface heat flux, Q, includes flux of sensible heat, Q_{se}, latent heat, Q_{la}, long-wave radiation, Q_{lw} and the fraction, η, of short-wave solar radiation, Q_{sw}, that is absorbed at the surface,

$$Q = Q_{se} + Q_{la} + Q_{lw} + \eta Q_{sw}. \tag{11}$$

The sensible and latent heat fluxes are calculated from the 10 m wind speed, $|U_{10}|$, the air temperature at the sea surface, T_{ss}, together with the air temperature, T_a, and the relative humidity, R_q, at standard level. T_{ss} is assumed to equal the sea-surface temperature of the ocean (Gill, 1982),

$$Q_{se} = \rho_a c_{pa} C_H |U_{10}|(T_{ss} - T_a), \tag{12}$$

$$Q_{la} = \rho_a L_v C_E |U_{10}|(q_{ss} - q_a). \tag{13}$$

ρ_a is the density of air, c_{pa} is the heat capacity of air, C_H and C_E are bulk transfer coefficients, L_v is the latent heat of vaporization and q_{ss} and q_a are the specific humidities at the sea surface and at the standard level, respectively.

At the sea surface the air is assumed to be saturated and at the reference level a constant relative humidity is assumed. The specific humidity can be calculated from the temperature and the saturation vapour pressure, e_w, which in turn also is a function of the temperature (Gill, 1982),

$$q = R_q \frac{e_w}{\rho_a R_v (T + 273.15)}, \tag{14}$$

$$\log_{10} e_w = \frac{0.7859 + 0.03477T}{1 + 0.00412T}, \tag{15}$$

where R_v is the gas constant of vapour. q_a is thus calculated from $T = T_a$ and q_{ss} is calculated from $T = T_{ss}$.

The long-wave radiation is calculated by (Gill, 1982)

$$Q_{lw} = 0.985\sigma(T_{ss} + 273.15)^4\left(0.39 - 0.05q_a^{1/2}\right)\left(1 - 0.6n_c^2\right), \tag{16}$$

where σ is the Stefan Boltzman constant and n_c is the cloud cover fraction. All temperatures are given in degrees Celcius. The short-wave radiation is calculated by (Gill, 1982)

$$Q_{sw} = Q_I(1 - \gamma)(1 - 0.7n_c)\cos(\phi), \tag{17}$$

where Q_I is the solar radiation that penetrates to the lower atmosphere, γ is the albedo and ϕ is the altitude of the sun.

The model is forced with data of 10 m wind. From these, the water side sea-surface friction velocity, u_*, is calculated. The forcing is one-way only, leaving the atmosphere unaffected by the momentum fluxes to the ocean. Initially the ocean is at rest and the temperature and salinity profiles are according to observations. The model is allowed to spin up for a time sufficient for the mixed layer depth to reach a similar value to what can be estimated from the observations. During the spin up period the temperature and salinity profiles are kept unchanged.

See the Appendix for further details about the model.

4. Model validation

The model is tested in two ways. First, the model is compared with the result of an analytical solution. This case is Kato and Phillips' classical grid stirring experiment. The water column is initially at rest and has a homogeneous buoyancy frequency, N. At the surface there is a constant friction velocity, u_*. According to Price (1979) the mixed layer depth, d, can be calculated as

$$d = 1.047u_*(t/N)^{1/2}. \tag{18}$$

The mixed layer can be defined according to some level of turbulent kinetic energy, k. The threshold $k > 10^{-6}$ m^2 s^{-2} is chosen. However, the choice of definition of the mixed layer is not crucial. Changing the threshold with a factor of 10 or using stratification as criterion does not fundamentally change the result. In Fig. 2 it can be seen that the modelled mixed layer depth follows eq. (18) closely. We tried alternative turbulence models, including two-equations $k-\epsilon$ and $k-\omega$ models. They tended to underestimate the mixed layer depth during the first hour of simulation with up to 1 m difference.

Second, the model is compared with the result of observations and previous simulations. This case is the tropical hurricane Felix. Its passage close to the Bermuda Testbed Mooring (BTM) in August 1995 is one of the few cases where there exist atmospheric observations and also hydrological observations, both before and after the passage. To the best of our knowledge there exist no similar observations of polar lows. Zedler et al. (2002) presented a detailed analysis of the Felix case, together with several numerical simulations.

The forcing wind and temperatures are observations taken from the BTM site, measured at approximately 4.2 m above the sea surface. The wind is adjusted to a 10 m value, $|U_{10}|$, using a logarithmic velocity profile. After that a second adjustment is done, to $|U_{10w}|$, accounting for the effect of waves, see Appendix.

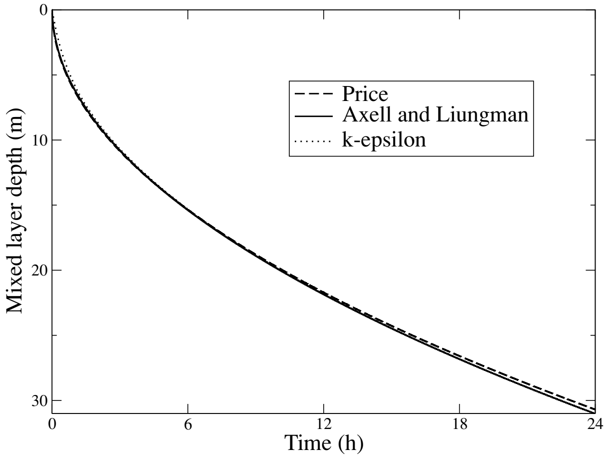

Fig. 2. Temporal evolution of the mixed layer depth in the homogeneous stratification test case. The dashed line show equation 18, the solid line show modelled result. In this case $N_0 = 10^{-2}$ s^{-1} and $u_* = 10^{-2}$ m s^{-1}.

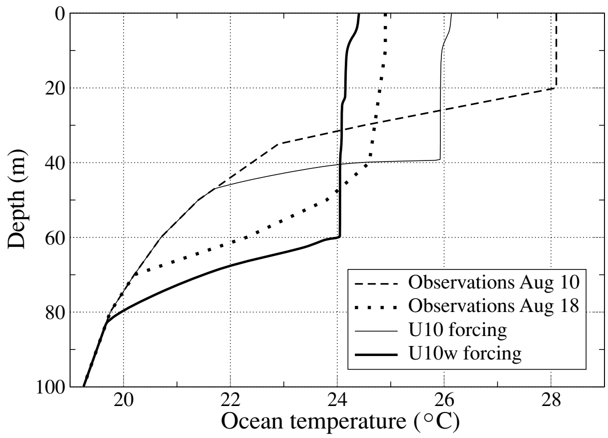

Fig. 3. Temperature profiles in the hurricane Felix test case. Thick line is the forcing wind adjusted for wave distortion, thin line is the forcing wind without adjustment.

Figure 3 show the temperature profiles from our simulation of the Felix case. It can be seen that the wind forcing without adjustment for the wave effect results in too little mixing. Adjusting for this effect results in too much mixing, but the temperature profile is still in better agreement with the observations. The simulations by Zedler et al. (2002) shown in their Fig. 4 bracket our simulation using $|U_{10}|$ forcing. They report that adjusting the wind forcing accounting for the effect of waves results in a mixed layer depth 12–19 m deeper than observations. This is in good agreement with the result from our simulation.

The result from our simulations of the Felix case using $k-\epsilon$ and $k-\omega$ models did not produce significantly different result from the Axell and Ljungman model. To conclude: we believe our model is on par with other well-designed models.

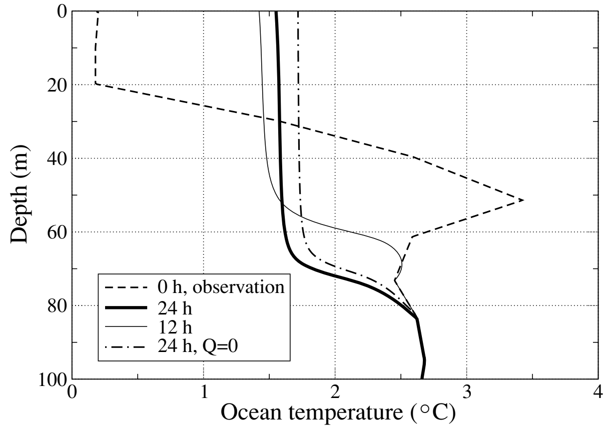

Fig. 4. Temperature profiles at station 1.

5. Entrainment in the Nordic Seas

We now turn to our region of interest, the Nordic Seas. The ocean model is initialized with temperature and salinity observations from the two stations marked with numbers on Fig. 1. These observations are chosen for their pronounced temperature inversion, but as shown in Section 2 this is not a unique or uncommon in feature in Fig. 1. The model is forced with a constant 25 m s^{-1} wind. The atmosphere is assumed to retain a constant temperature 7 °C lower than the initial SST. A relative humidity of 70% is assumed. The result from the two simulations are displayed in Figs. 4–8.

Figures 4 and 5 show temperature profiles. The initializing temperature observations (dashed lines) reveal 10–20 m deep surface layers. Beneath the surface layers the temperature increases several degrees to maxima situated at around 50 m depth. After 24 h (thick solid lines) of wind induced mixing the surface layers have deepened to more than 80 m, consuming the temperature maxima. The resulting SST are higher than the original SST, but lower than the temperature maxima.

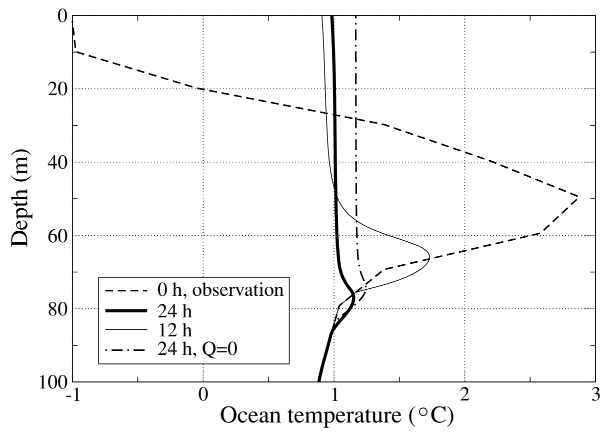

Fig. 5. Temperature profiles at station 2.

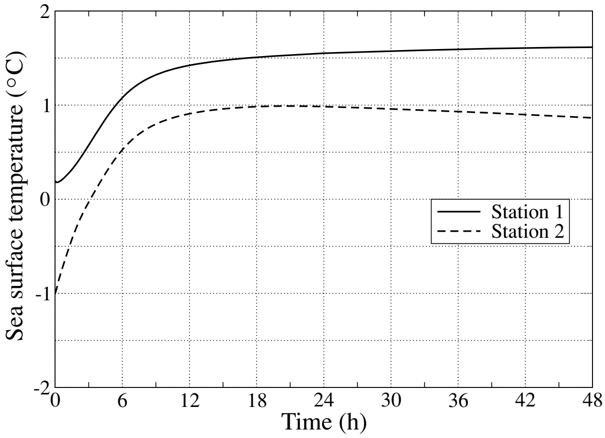

Fig. 6. Sea-surface temperature at station 1 and 2.

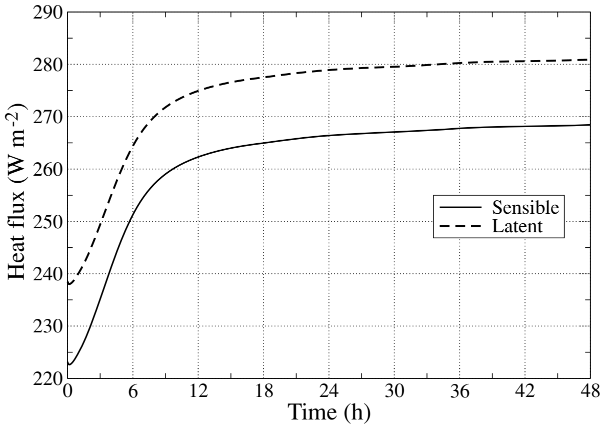

Fig. 7. Heat fluxes (W m^{-2}) at station 1.

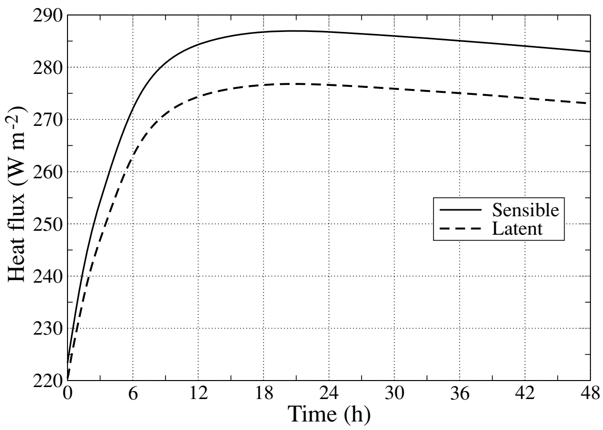

Fig. 8. Heat fluxes (W m^{-2}) at station 2.

At station 1, the water beneath the surface layer after 24 h is still around 1 °C higher than the SST, see Fig. 4. This means that continued deepening of the surface layer can lead to a further increase of the SST. At station 2 the water beneath the surface layer is after 24 h of similar temperature as the SST, see Fig. 5. Continued deepening of the surface layer can not lead a further increase of the SST here.

The thin solid lines show the results after 12 h of simulation. They reveal that during these hours the surface layers deepen to around 50 m. During the following 12 h the surface layers deepen around 15 m more, but that has a rather limited effect on the SST.

The dash–dotted lines show the results of simulations without heat fluxes through the ocean surface. They are included to display how limited the effect of the heat fluxes on the SST is, compared to the effect of entrainment of warmer water into the surface layer. The effect of the heat fluxes on the mixed layer depth is evidently negligible.

Figure 6 shows how the SST evolve in time. The response of the SST of the entrainment of warmer water into the surface layer is greatly influenced by the shape of the upper ocean temperature profile. The response can be studied by dividing it into three phases:

1. Increasing response, indicated by an accelerating SST. In a SST graph it will correspond to a climbing and upward bending curve. There is a time lag between the deepening of the surface layer and the complete mixing of the entrained warmer water all the way to the surface. Initially the entrained water is brought into a boundary layer at the bottom of the surface layer. This layer can be seen in Figs. 4 and 5. Water from the boundary layer is eventually mixed up into the greater surface layer, affecting the SST. The response on the SST is increasing because the volume and the temperature of the water being mixed out of the boundary layer into the greater surface layer is increasing. The increasing response is also caused by the increasing temperature difference between the surface layer and the water being entrained into the boundary layer. The first hours of simulations at station 1 can be defined as belonging to this phase, see the solid line in Fig. 6. At station 2, the shallower surface layer, together with an equally steep temperature gradient underneath, makes this period extremely short and not distinguishable in the dashed line in Fig. 6.

2. Decreasing response, indicated by a slowing increase of SST. In a SST graph it will correspond to a climbing but downward bending curve. The entrainment of warmer water into the surface layer will necessarily make that layer deeper and warmer. A constant increase of the SST will demand constantly greater volumes of water, with constantly higher temperatures, from the boundary layer at the bottom of the surface layer. At station 1 this phase starts after approximately three hours and continues for the remainder of the simulation, see the solid line in Fig. 6. At station 2 this phase starts almost immediately and continuous for approximately 18 h, see the dashed line in Fig. 6.

3. Exhausted response, indicated by a constant or decreasing SST. Eventually the entrainment of warm water into the surface layer can not outpace the heat fluxes to the atmosphere. This

happens when the water underneath the mixed layer no longer has a sufficient temperature difference to the layer above, as is the case at station 2 after 24 h, see the solid line in Fig. 5. Eventually this will always happen, as the wind induced mixing fails to further deepen the surface layer by continuously entraining more water from the layer underneath. In this phase the surface heat flux lead to a decreasing SST, as it does at station 2 during the second half of the simulation time. A deepened mixed layer will however mean that the effect of the fluxes are distributed over a large depth and causes only a modest change at the surface.

What we find is that on a short timescale, during high wind conditions, the vertical mixing dominates over the surface heat fluxes in determining the SST. This is true both in a tropical scenario, as shown in Section 4, and in a high latitude scenario, as shown here. In the tropical scenario, where the surface layer always is warmer than the water underneath, a hurricane will inevitably leave a colder sea surface in its track. In a high latitude scenario, where the surface layer may be colder than the deeper layer, a polar low may leave a warmer sea surface in its track.

The heat fluxes to the atmosphere do result in a net cooling, as can be seen in Figs. 4 and 5 by comparing the simulations with and without surface heat fluxes. The net cooling results in both of the simulations in surface layers with around 0.2 °C lower temperature after 24 h.

Long-wave radiation contributes to the heat flux from the ocean. Its magnitude is however smaller, around 70 W m^{-2} at both stations, and hardly influenced at all by SST changes of only a few degrees. The mean short-wave solar radiation to the ocean is at both stations less than 30 W m^{-2}.

Since the conditions in the atmosphere are kept constant, the higher SST will necessarily lead to higher heat fluxes from the ocean to the atmosphere. The increase is rather dramatic during the first 6 h of simulations and after that the fluxes remain at the high level, see Figs. 7 and 8. It is noteworthy that the sensible and latent heat fluxes are of approximately the same magnitude. This is contrary to tropical scenarios, where the latent heat flux usually is three times or more larger than the sensible. It is also noteworthy that the pattern of the effect of the SST on the surface fluxes is not strongly dependant on the constants chosen for the atmosphere here. Other values for humidity, air temperature and the wind result in other levels of heat fluxes, but the pattern of response to the SST changes remains similar to what is shown in Figs. 7 and 8.

Two immediate questions can be raised here. First, what will be the short-term response by the atmosphere? This may include changes in the humidity and the atmosphere temperature, which will dampen the effect of the SST change on the heat fluxes to the atmosphere. It may also include a deepening of the energy potential, by increasing the temperature difference between the planetary boundary layer and the tropopause temperatures. This may intensify the weather system, enhancing both the effect of the SST change on the heat fluxes and the entrainment of deeper water into the surface layer. Second, what will be the long-term effect of this type of short timescale events? The increased heat fluxes may have an impact on the overall climatology of the region. Investigations by Korty et al. (2007) and Pasquero and Emanuel (2007) indicate that the vertical entrainment in the wake of tropical cyclones do have a an impact on the climate. This question becomes especially intriguing when it is kept in mind that the region is the entrance into the Arctic Ocean and of importance for densification and eventual deep water formation. Answering these questions does however not fall within the scope of this paper.

6. Observational evidence of surface warming

On 18 December 2004, a polar low is observed in the Norwegian Sea near the Lofoten island in Northern Norway. The polar low develop during a cold-air outbreak during the night of 17–18 December. At 0200 UTC, a disturbance is visible in the satellite image from NOAA, located around 71°N, 5°E. As the disturbance moves southeast, a cyclone develops. Figure 9 shows the satellite image for 1011 UTC on 18 December. The cyclone centre was then around 69°30′N, 7°30′E. During the day, the polar low moved to the southeast. At 2117 UTC, the polar low was centred around 67°30′N, 12°30′E, which is outside the Lofoten islands (see Fig. 10). At this time, the polar low started to landfall and gradually weakened. During the 11 h between the two satellite images the polar low moved approximately 270 km, corresponding to a speed around 7 m s^{-1}. Let us assume that the azimuthal wind is axisymetric around the cyclone centre. Then the real wind speed will be 14 m s^{-1} higher on the right side of the path of the cyclone centre compared to left side.

The ocean bathymetry outside the Lofoten island is characterized by a particularly steep continental edge. From a narrow continental shelf with approximately 200 m depth, the depth increases to about 3000 m less than 100 km from land. It is well known that the North-Atlantic current is narrower and more intense due to topographic steering in this area. To analyse the oceanic response to the polar low described above, satellite microwave data, AMSRE, have been used. The data were downloaded from the Remote Sensing Systems web-page (http://www.remss.com/), where daily optimally analysed global SST data from 2002 is available. The advantage of microwave satellite data is the fact that they can see through clouds and are not restricted to cloud-free conditions.

Figure 11 shows the sea-surface temperatures for 17 December 2004. The surface temperatures in the area of the cyclogenesis is about 6 °C. The waters over the continental shelf and edge are slightly warmer with temperatures about 7 °C and some spots with temperatures up to 8 °C. Surface temperatures exceeding 8.5 °C are mostly located south of 65°N. Figure 12 depicts the surface temperatures for the 18 December. The most striking feature here is the large SST increase in the area

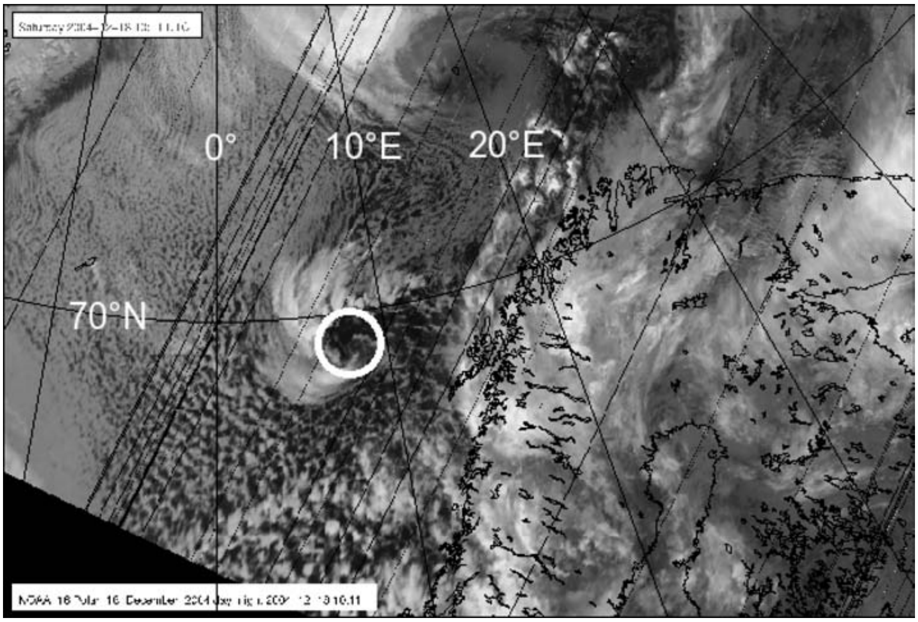

Fig. 9. NOAA Satellite picture for 18 December 2004, 1011 UTC. The centre of the polar low is marked with a white circle.

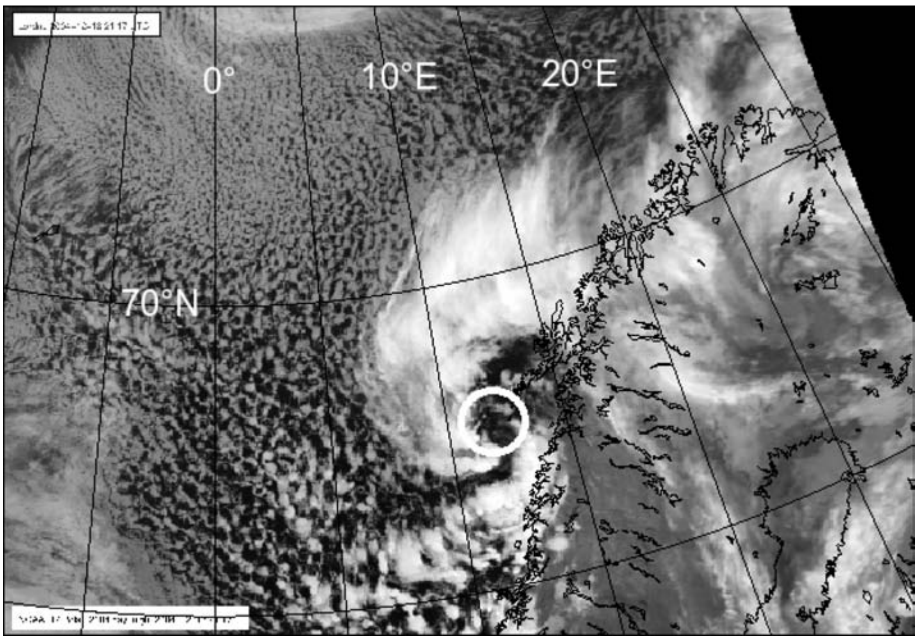

Fig. 10. NOAA Satellite picture for 18 December 2004, 2117 UTC, shortly before landfall. The centre of the polar low is marked with a white circle.

affected by the polar low. Figure 13 shows the SST difference between the 17 and 18 December, positive values indicating surface warming. The area with the highest increase in SST, up to 2°, is found southwest of the Lofoten island. This coincides remarkably well with the position of the convective clouds of the polar low as seen in the satellite pictures. Based on the SST observations from the 17 December, the day before the polar low event, it is difficult to imagine that this could be caused by horizontal advection of surface waters. The two remaining possibilities are then either entrainment of warm waters from below the surface or contaminated satellite data. To assess the quality of the satellite data under these conditions is beyond the scope of this investigation. However, examining the satellite SST data for the days after the polar low event (not shown here), reveals the presence of a warm pool of surface waters in the same area for several days. We take this as evidence that the surface warming is a real feature and not an artefact of the observation platform.

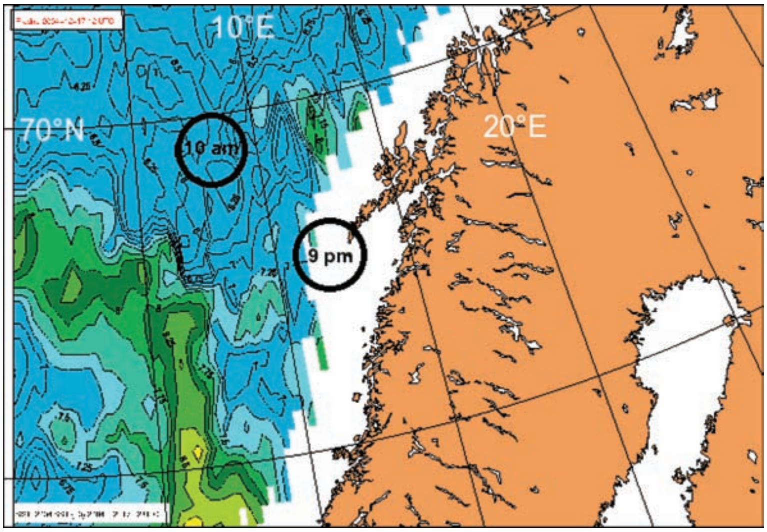

Fig. 11. SST from optimally interpolated satellite microwave observations (AMSRE) for 17 December 2004. The centre of the polar low as shown by the satellite pictures in Fig. 9 (10 am) and Fig. 10 (9 pm) is marked with black circles.

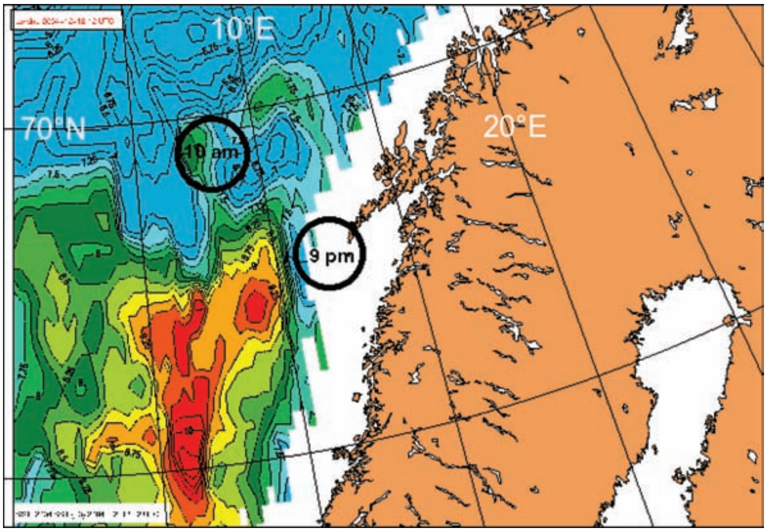

Fig. 12. SST from optimally interpolated satellite microwave observations (AMSRE) for 18 December 2004. The centre of the polar low as shown by the satellite pictures in figure 9 (10 am) and Fig. 10 (9 pm) is marked with black circles.

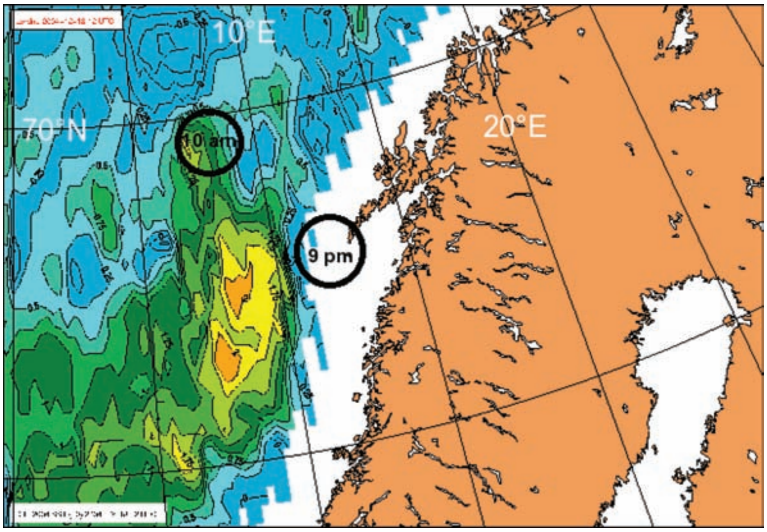

Fig. 13. Difference between SST values the 17th and the 18th December 2004. Positive numbers indicating a surface warming. The centre of the polar low as shown by the satellite pictures in Fig. 9 (10 am) and Fig. 10 (9 pm) is marked with black circles. Note that the location of the maximum temperature difference is to the right of the path of the polar low and over the North Atlantic Current, as shown in Fig. 1.

7. Summary and concluding remarks

The possibility of surface warming due to intense vertical mixing in the upper ocean has been investigated. The main basis for the hypothesis is the frequently observed oceanic temperature inversion in the wintertime hydrography of the North-Atlantic. Strong surface winds from polar lows may induce sufficient vertical mixing for the subsurface warm core to entrain the ocean surface, and hence, lead to a warming of the ocean surface. If the surface warming is sufficiently rapid, this could be a potential positive feedback mechanism for the atmosphere, leading to a more intense cyclone.

Temperature inversions in wintertime CTD-soundings from the Nordic Seas are a very common feature during winter, in particular for areas influenced by the NAC and Arctic water. In our study, observations collected in the HydroBase2 database were used to demonstrated the presence of a subsurface warm core in almost half of the hydrographic wintertime soundings from the region. It came to a great surprise to us then that hardly any documentation exist of this in the literature.

The timescale considered here is from the order of a few hours to a maximum of two days. Within this time-range, horizontal advection in the ocean is of limited significance. Changes of surface temperatures on this scale must be dominated by either vertical mixing of or cooling/warming by surface fluxes. As polar lows almost exclusively exists during winter, short-wave solar radiation is negligible. Although the latent and sensible heat fluxes are large during cold-air outbreak, they could only account for temperatures changes of about one tenth of a degree on the timescale considered here. The dominant mechanism for large temperature changes is the turbulent vertical mixing induced by extremely strong wind forcing. It has been demonstrated here that if a relatively shallow subsurface warm core is present, surface warming of one degree can be achieved within a few hours. A point to stress here is that the surface entrainment is not affected by Ekman pumping to any significant degree. This has also been demonstrated by Zedler et al. (2002) and by Emanuel et al. (2004). In the model used here, horizontal dependency, and hence Ekman pumping, is ruled out. Turbulent diffusion is then the only mechanism left for vertical displacement. The reader should note however that during out investigation, we also compared the Ekman pumping to the vertical mixing, using and axisymmetric model that included vertical turbulent mixing and horizontal divergence. We found that the vertical displacement from Ekman pumping was at least one order of magnitude smaller that the turbulent mixing and could not contribute on such short timescales.

Strong signal of surface warming in connection with polar lows was observed in a case near the Lofoten islands off the coast of Northern Norway. This is an area where the NAC is narrower and more pronounced than elsewhere. The reason for this is the particularly steep continental edge found in this area. The polar low developed during cold-air outbreaks from the northwest and intensified considerably in the warm surface areas influenced by the NAC. Optimally interpolated data from microwave sensors showed a surface warming of as much as 2 °C under the polar low track. Horizontal advection could be excluded as source for such warm waters. Further evidence that this is caused by vertical mixing induced by the strong winds are the fact that the maximum temperature increase in the satellite observations fits precisely to where the satellite picture indicates strongest deep-convection. However, the possibility that this is an artificial effect of the observation system can not be entirely excluded.

Based on the results presented here, we conclude that rapid surface warming by turbulent mixing is possible during strong wind events such as polar lows. This is most likely to happen in ocean areas influenced by the warm waters of the NAC or Arctic water. Whether this can act as a positive feedback mechanism of any importance on the cyclone intensity remains to be investigated. A surface warming of one degree or more will enhance the surface heat fluxes considerably. This could be seen as a parallel to deep surface layer and warm core rings in the tropics, and the role they play for the development of hurricanes. The question is however, if the cyclone moves slowly enough to be affected by this. The life-time of most polar lows is relatively short, since the cyclone moves rather fast and usually landfalls after a few hours. To answer this, further investigation is needed.

8. Acknowledgements

This research was partly funded by The Research Council of Norway trough the projects ArcChange, contract 178577/S30, and IPY-THORPEX, contract 175992/S30. The contribution from Torsten Hanson was funded by the European Commission through a research fellowship under the Mod&Obs project, contract MRTN-CT-2005-019369. We thank Professor Jan Erik Weber for support and valuable discussions.

9. Appendix

In eq. (9), the turbulence production from shear, P_s, and from buoyancy production, P_b, are calculated by

$$P_s = K_M \left[\left(\frac{\partial u}{\partial z} \right)^2 + \left(\frac{\partial v}{\partial z} \right)^2 \right] \tag{A1}$$

and

$$P_b = -K_H N^2. \tag{A2}$$

N^2 is the buoyancy frequency squared,

$$N^2 = -\frac{g}{\rho_0} \frac{\partial \rho}{\partial z}, \tag{A3}$$

where g is acceleration due to gravity, ρ is density and ρ_0 is the mean density. ϵ in eq. (9) is the dissipation rate. By dimensional arguments it can be calculated by

$$\epsilon = \left(c_\mu^0\right)^3 \frac{k^{3/2}}{l}, \tag{A4}$$

where c_μ^0 is the value of c_μ in the logarithmic layer close to a boundary and l is the mixing length.

Following Axell and Liungman (2001), the mixing length is calculated with an algebraic expression based on the geometric length scale, l_g, and the buoyancy length scale, l_b,

$$\frac{1}{l^2} = \frac{1}{l_g^2} + \frac{1}{l_b^2}, \tag{A5}$$

$$l_g = \kappa(d + z0), \tag{A6}$$

$$l_b = c_b \frac{k^{1/2}}{N}, \tag{A7}$$

where κ is the von Karman constant, d is the distance to the closest boundary, z_0 is the roughness length and c_b is a constant. In case of strong stable stratification, $N^2 < -c_b^2\, k/l_g^2$, eq. (A5) will fail. An alternative expression is obtained by multiplying eq. (A5) by $l^2\, l_g^2$,

$$l^2 = l_g^2 - \frac{l^2 l_g^2}{l_b^2}. \tag{A8}$$

This expression is used when $N^2 < 0$. For moderate stratification, stable or unstable, eqs (A5) and (A8) are equivalent. The reader may note that l appears on both sides in eq. (A8), which is solved numerically by using the value from the old time step on the right-hand side.

One fraction, η, of the solar radiation, Q_{sw}, is assumed to be a boundary heat flux and the rest, Γ in eq. (5), a heat source in the upper part of the water column,

$$\Gamma = (1 - \eta)\frac{Q_{sw}}{\rho c_p} e^{-\beta(H-z)}, \tag{A9}$$

where c_p is the heat capacity of water and β is the extinction coefficient.

The surface stress is calculated from the 10 m wind, $\vec{U}_{10}$,

$$u_*^2 = \vec{U}_{10}^2 C_D \frac{\rho_a}{\rho}, \tag{A10}$$

where C_D is the drag coefficient, calculated by the Large and Pond (1981) formula

$$C_D = 1.2 \times 10^{-3}, \quad |\vec{U}_{10}| \le 11 \text{ m s}^{-1}, \tag{A11}$$

$$C_D = (0.49 + 0.065|\vec{U}_{10}|) \times 10^{-3}, \quad |\vec{U}_{10}| > 11 \text{ m s}^{-1}. \tag{A12}$$

It should be noted that this parametrization is reported to be valid up to 25 m s^{-1}, which is less than the maximum wind during our cases. The two horizontal components of the friction velocity is calculated according to

$$u_{*x}^2 = \cos(\theta) u_*^2 \qquad \text{and} \qquad u_{*y}^2 = \sin(\theta) u_*^2, \tag{A13}$$

where θ is the wind direction.

The logarithmic wind profile may be distorted by waves. Large et al. (1995) suggested that when low level wind measurements are adjusted to 10 m wind, the wave distortion should be accounted for. They derived an empirical relationship for how measurements at 4.5 m should be adjusted a second time to account for wave distortion.

$$|U_{10w}| = |U_{10}|, \quad |U_{10}| \le 9.05 \text{ m s}^{-1}, \tag{A14}$$

$$|U_{10w}| = 1.53 \cdot |U_{10}| - 4.80, \quad |U_{10}| > 9.05 \text{ m s}^{-1}. \tag{A15}$$

The numerical computations have been conducted using the equation solver PROBE (Svensson, 1998), which in its 2002 version features an option for using the Axell and Liungman Axell and Liungman (2001) approach. The stability functions for K_M and K_H are, according to Axell and Liungman,

$$c_\mu = \frac{0.556 + 0.108 R_t}{1 + 0.308 R_t + 0.00837 R_t^2} \tag{A16}$$

and

$$c'_\mu = \frac{0.556}{1 + 0.277 R_t}, \tag{A17}$$

Table 5. Model constants

Constant	Symbol	Value
Grid size	Δz	0.25 m
Time step	Δt	30 s
Reference density	ρ_0	1000 kg m^{-3}
Density of air	ρ_a	1.3 kg m^{-3}
Roughness length	z_0	1.0 m, $z = H$
Roughness length	z_0	0.03 m, $z = 0$
Model constant	c_b	0.35
Bulk transfer constant	C_E	1.5×10^{-3}
Bulk transfer constant	C_H	0.97×10^{-3}
Stefan Boltzmann's const	σ	5.7×10^{-8} W m^{-2} K^{-4}
Heat of vaporization	L_v	2.257×10^3 J kg^{-1}
Gas constant, vapour	R_v	461.5 J kg^{-1} °C^{-1}
Heat capacity, air	c_{pa}	1012 J kg^{-1} °C^{-1}
Heat capacity, water	c_p	4200 J kg^{-1} °C^{-1}
Solar radiation, lower atm.	Q_I	1367 W m^{-2}
Albedo	γ	0.1
Cloud cover fraction	n_c	0.5
Absorption fraction	η	0.5
Extinction coefficient	β	0.25
Wave factor	α	100

where R_t is the turbulent Richardson number,

$$R_t = \frac{k^2 N^2}{\epsilon^2}. \tag{A18}$$

Model constants are specified in Table 5.

References

Axell, L. B. and Liungman, O. 2001. A one-equation turbulence model for geophysical applications: comparison with data and the $k - \epsilon$ model. *Environ. Fluid Mech.* **1**, 71–106.

Brink, K. H. 1989. Observations of the response of thermocline currents to a hurricane. *J. Phys. Ocean.* **19**, 1017–1022.

Craig, P. D. and Banner, M. L. 1994. Modeling wave-enhanced turbulence in the ocean surface layer. *J. Phys. Ocean.* **24**, 2546–2559.

Ekman, V. W. 1905. On the influence of of the earth's rotation on ocean currents. *Ark. Mat., Astron. Fys.* **2**(11), 1–52.

Emanuel, K. A. and Rotunno, R. 1989. Polar lows as arctic hurricanes. *Tellus* **41A**, 1–17.

Emanuel, K. A., DesAutels, C., Holloway, C. and Korty, R. 2004. Environmental control of tropical cyclone intensity. *J. Atmos. Sci.* **63**, 843–851.

Gill, A. E. 1982. *Atmosphere and Ocean Dynamics*, Academic Press, London, pp 662.

Hong, X., Chanh, S. W., Raman, S., Shay, L. K. and Hodur, R. 2000. The interaction between hurricane Opal (1995) and a warm core ring in the Gulf of Mexico. *Mon. Wea. Rev.* **128**, 1347–1365.

Kafatos, M., Donglian, S., Gautam, R., Boybeyi, Z. and Yang, R. 2006. Role of anomalous warm gulf waters in the intensification of Hurricane Katrina. *Geophys. Res. Let.* **33**, L17802.

Korty, R. L., Emanuel, K. A. and Scott, J. R. 2007. Tropical cyclone-induced upper ocean mixing and climate: application to equable climates. *J. Clim.*, in press.

Large, W. G. and Pond, S. 1981. Open ocean momentum flux measurements in moderate to strong winds. *J. Phys. Ocean.* **11**, 324–336.

Large, W. G. Morzel, J. and Crawford, G. B. 1995. Accounting for surface wave distortion of the marine wind profile in low-level ocean storms wind measurements. *J. Phys. Ocean.* **25**, 2959–2971.

Nordeng, T. E. and Rasmussen, E. A. 1992. A most beatiful polar low. A case study of a polar low development in the Bear Island region. *Tellus* **44A**, 81–99.

Pasquero, C. and Emanuel, K. A. 2007. Tropical cyclones and transient upper ocean warming. *J. Clim.*, in press.

Price, J. F. 1979. On the scaling of stress-driven entrainments. *J. Fluid. Mech.* **90**, 509–529.

Price, J. F. 1981. Upper ocean response to a hurricane. *J. Phys. Ocean.* **11**, 153–175.

Price, J. F. 1983. Internal wave wake of a moving storm. Part I: scales, energy budget and observations. *J. Phys. Ocean.* **13**, 949–965.

Price, J. F., Sandford, T. B. and Forristall, G. Z. 1994. Forced stage response to a moving hurricane. *J. Phys. Ocean.* **24**, 233–260.

Rasmussen, E. A. and Turner, J. 2003. *Polar Lows*, Cambridge University Press, Cambridge, pp 612.

Sanford, T. B., Black, P. G., Haustein, J. R., Feeney, J. W., Forristall, G. Z., and co-authors. 1987. Ocean response to a hurricane. Part I: observations. *J. Phys. Ocean.* **17**, 2065–2083.

Schade, L. R. and Emanuel, K. A. 1999. The ocean's effect on the intensity of tropical cyclones: results from a simple coupled atmosphere ocean model. *J. Atmos. Sci.* **56**, 642–651.

Shapiro, M. A., Fedor, L. S. and Hampel, T. 1987. Research aircraft measurements of a polar low over the Norwegian Sea. *Tellus* **39A**, 272–306.

Shay, L. K., Goni, G. J. and Black, P. G. 2000. Effects of a warm oceanic feature on hurricane Opal. *Mon. Wea. Rev.* **128**, 1366–1382.

Svensson, U. 1998. *PROBE, Program for Boundary layers in the Environment. System Description and Manual*, Report Oceanography No. 24, Swedish Meteorological and Hydrological Institute, SE-601 76, Norrkoping, Sweden,

Tennekes, H. and Lumley, J. L. 1972. *A First Course in Turbulence*, The MIT Press, Cambridge, Massachusettes, pp 300.

Zedler, S. E., Dickey, T. D., Doney, S. C., Price, J. F., Yu, X., and co-authors. 2002. Analyses and simulations of the upper ocean's response to Hurricane Felix at the Bermuda Testbed Mooring site: 13–23 August 1995. *J. Geophys. Res.* **107**, 1–29.